CHAPTER-5

BIFUNCTIONAL CATALYTIC BEHAVIOR OF $La_{0.5}Sr_{0.5}Fe_{0.5}Ti_{0.5}O_3$

Uma Sharma, Priyanka A. Jha, Pardeep K. Jha, Prabhakar Singh, Highly efficient and robust bifunctional environmental friendly $LaSrFeTiO_3$ catalyst for H2/O2 fuel cells, (Under Review)

CHAPTER 5: Bifunctional catalytic behavior of $La_{0.5}Sr_{0.5}Fe_{0.5}Ti_{0.5}O_3$

5.1 Introduction

Charge dynamics and the electrochemical studies in different pH media of $SrTiO_3$ have been discussed in chapter 4. Also, it has been reported that the high catalytic involvement occurred in the neutral medium compared with the other two: acidic and basic media.

This chapter explores the bifunctional catalytic behavior of $La_{0.5}Sr_{0.5}Fe_{0.5}Ti_{0.5}O_3$ (LSFT) which is formed by co-substitution of Sr and Ti. The structural and electrical properties are the same as discussed in Chapter 3. Here, electrochemical measurements of LSFT were performed in three pH medium (Alkaline, Neutral, Acidic). A higher current density is observed in the OER and ORR regimes with higher stability in the neutral media compared to basic and acidic. The cyclic stability of the LSFT has been studied and it remains stable for 600 cycles in the neutral medium. The chronopotentiometry stability of the LSFT is also observed in all three media and remains stable for 1500 h in the neutral medium. The electrochemical reversibility/irreversibility and transient time decay are also discussed in this chapter.

5.2 Experimental Procedure

The samples with composition $La_{0.5}Sr_{0.5}Fe_{0.5}Ti_{0.5}O_3$ (LSFT) have been prepared using conventional Solid State Reaction (SSR) Method. Lanthanum (III) oxide (La_2O_3), Iron (III) oxide (Fe_2O_3), and Strontium carbonate ($SrCO_3$), Titanium (IV) oxide (TiO_2) (all from Alpha Aesar with purity more than 99%) were used to synthesized sample. Initially, the pre-defined stoichiometric amount of highly purified dry starting materials was weighed and all oxides

were intimately mixed by grinding it finely with a mortar and pestle using acetone as a mixing medium around 2−3 h for preparing each of the sample powders. Then all the sample powders have been preheated at 300 ℃ for 4 h in a hot air oven. After preheating, the powders are again ground thoroughly. Further grounded samples were subjected to calcination at 1200 ℃ for 2 h with the heating rate at 5 ℃ /min in the muffle furnace for the completion of the reaction, phase formation and to get rid of impurities like carbonates etc.. Further calcined powders were used for the phase and structure determination by X-Ray Diffraction (XRD) instrument in the 2θ range from 10° to 80° with a step size of 0.02° at a scanning rate of 1 °/min with Cu-Kα radiation of wavelength (λ)~1.5405Å. From the calcined powders, three uniform pellets of each sample have been prepared for different types of characterization. For this, calcined powders were mixed with the prepared PVA binder solution by grinding it in a mortar and pestle. The resulting powder was made into circular pellets by applying pressure for one minute using a hydraulic press. These pellets have been sintered at 1300 ℃ for 2 h in the muffle furnace for grain growth with the same heating rate. Thereafter, the crystalline phase of the sintered sample was determined by XRD. Thereafter, platinum was pasted on both the faces of the pellets and cured at 750 ℃ for 20 min in the furnace for further measurements. The phase, structure, space group, atomic positions and occupancies of the components of the material is confirmed by Rietveld refinement of the X-ray diffraction data using FULLPROF software. We have taken valence band maximum (VBM) from X-ray photoelectron spectroscopy (XPS) and band gap value from UV-Visible spectroscopy. For the electrochemical studies of the samples cyclic voltammetry has been performed with a three-electrode electrochemical cell, where Ag/AgCl electrode is used as reference electrode, Pt wire as a counter electrode, and LSFT as working electrode, directly. 1M Sodium Sulphate (Na_2SO_4), a neutral solution with

pH=7, 1M KOH solution with pH=14 and 1M H_2SO_4 solution with pH=1 were being used as electrolytes. The chronopotentiometric stability of material was tested in three mediums for 1500 h. The Nernst equation used for the calculation of reference potential is[200]-

$$E_{RHE} = E_{cell} + 0.197 + 0.059pH \quad (5.1)$$

The estimations of highest occupied molecular orbitals (HOMO) and lowest unoccupied molecular orbitals (LUMO) were done with the empirical relation[200]-

$$E_{LUMO} = [(E_{red} - E_{1/2(ferrocene)}) + 4.8]\, eV \quad (5.2)$$

$$E_{HOMO} = [(E_{ox} - E_{1/2(ferrocene)}) + 4.8]\, eV \quad (5.3)$$

where $E_{1/2(ferrocene)} = 0.41\, V$.

5.3 Results and Discussion

5.3.1 Structural Analysis

The Rietveld refinement of XRD pattern of LSFT confirmed the orthorhombic phase with Pbnm symmetry and estimated lattice parameters (in Å) 5.530(3), 7.810(4), 5.555(1) (Fig.5.1(a))[201]. The band gap has been estimated using the Tauc relation (equation 3.1), with transmission mode, n = 0.48 showing direct transition is allowed (Fig. 5.1(b)). Fig. 5.1(b) inset shows the absorbance curve obtained from UV-visible spectrophotometer. Fig. 5.1(c) depicts the y-z plane of the LSFT structure. Here, in the structure, apical (4c Wyckoff site with 'm' symmetry) and axial O (8d Wyckoff site with '1' symmetry). The band gap estimated is 1.76 (± 0.09) eV and hence, conduction band minimum (CBM) lies at 1 eV while valence band maximum (VBM) lies at -0.76 eV suggesting VBM shifted towards EF (Fermi level) (Fig. 5.1(d)). The valence band edge has been determined using X-ray photoelectron spectroscopy

(refer to Fig. 5.2). Here, LSFT is a multi element system, and out of the constituent elements, Fe is the most corrosive element. On the other hand, Fe (1.83) has higher electronegativity than Ti (1.54), thus leading to the shifting of d-band towards Fermi level.

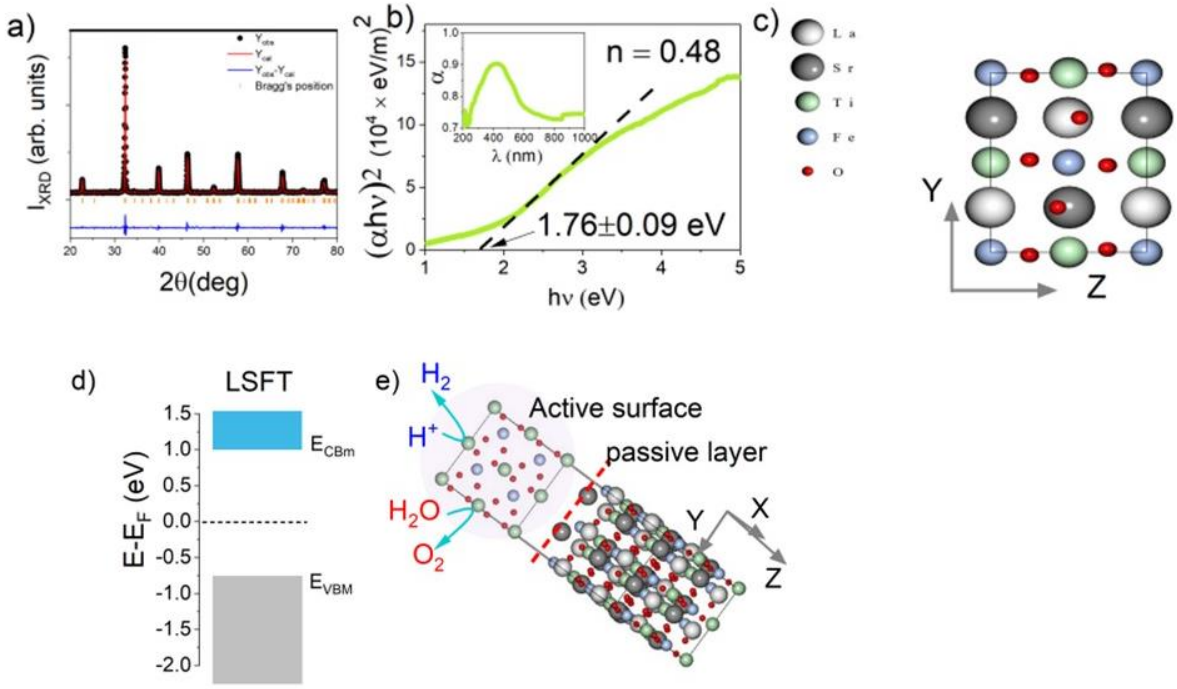

Figure 5.1 **(a)** XRD with Rietveld refinement of LSFT **(b)** Tauc plot to estimate band gap**,** inset shows the absorbance curve obtained from UV-Visible spectrophotometer, **(c)** depicts the y-z plane of the LSFT structure. **(d)** Band structure showing conduction band minimum (CBM) lies at 1 eV while valence band maximum (VBM) lies at -0.75 eV, **(e)** depicts the active surface containing Fe,Ti and O where (d-metal ligand) ORR occurs whereas OER takes place with the formation of passive layer containing La site.

Since, BO_6 octahedra of perovskites (metal-oxygen bond) controls surface binding energetics. With the removal of apical oxygen, surface layer has the coordination environment of BO_5 leading to the symmetry breaking and splitting of d-orbital[202]. This surface-adsorbate bonding is more favorable towards the vertical orientation of surface bound intermediates. This is the motivation of Fig. 5.1(e) where the active surface containing Fe, Ti and O where Fe (d-metal ligand) suggests HER/ORR (H_2/H^+ or H_2O/O_2) generation whereas OER (H_2O/O_2)

formation takes place with the formation of passive layer containing La site. Now, e_g orbital of transition metals overlaps with the tilted configuration of O_2 molecules and thus, tells the strength of binding of adsorbates with the surface. For the ORR, firstly, the electrons are injected to the catalyst populating the valence band up to highest occupied molecular orbital (HOMO). Then with the application of negative potential, electron energy raises the Fermi level above lowest unoccupied molecular orbital (LUMO) of the adsorbates[203]. After that electrons flow to the empty adsorbates and reduction takes place.

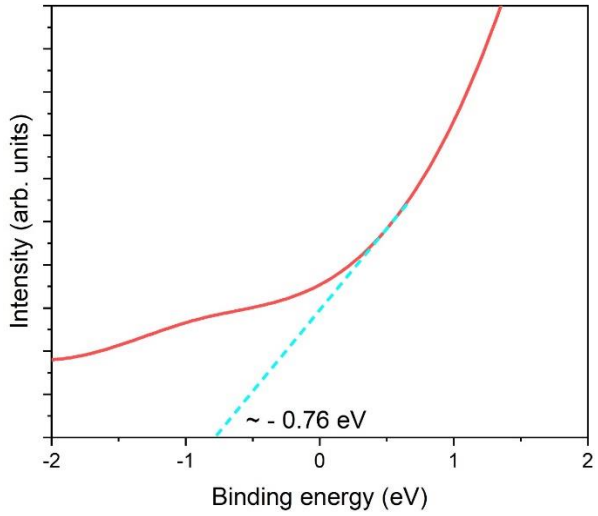

Figure 5.2 Valence band maximum (VBM) determination using X-ray photoelectron spectroscopy.

5.3.2 OER/HER

Figure 5.4(a) depicts that the peak current density (j_p) is three order higher, that is 0.2mA/cm^2 in neutral medium (pH = 7) as compared to alkaline medium (pH=14, j_p = 0.002 mA/cm^2). Here, in inset of Fig. 5.4(a), the shape of the curve is sigmoidal shaped at pH = 7 showing the catalytic regeneration while there is peak splitting in addition to sigmoidal shape at pH = 14. While, at pH=1 (Fig. 5.4(a) inset), j_p= 0.1 mA/cm^2 but there is no oxidation peak showing the depletion of oxidized species and reduction peak has shifted to 1st quadrant thus

leading to the merging of oxidation and reduction potentials. In order to elucidate more, J-V curves with the variation of scan rate have also been studied (refer to Fig. 5.3). The anodic and cathodic peak potential difference, ΔE_p > 180 mV with the variation of scan rate suggesting multiple electron processes at pH = 7[158]. At pH=1, ΔE_p > 180 mV for slowest (10 mV/sec) scan rate but oxidation peak diminishes at higher scan rates suggesting irreversible chemical reaction[158][204].

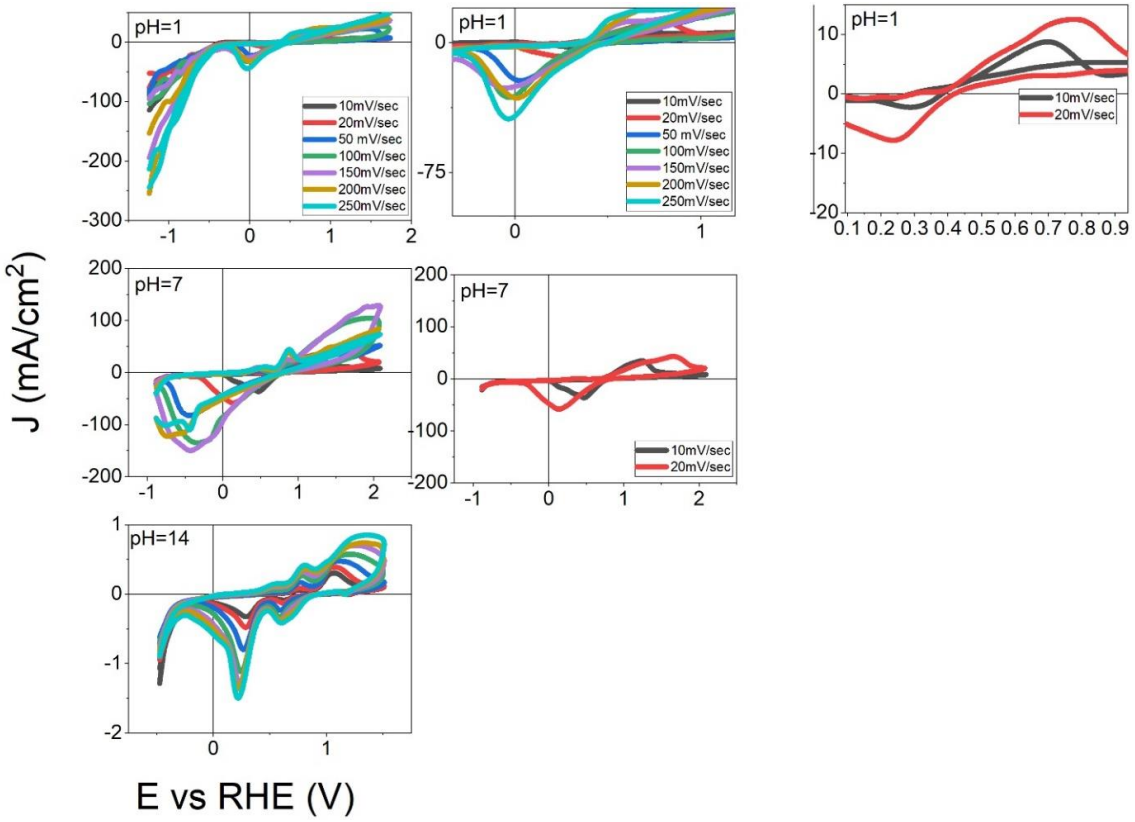

Figure 5.3 Cyclic voltammograms with the variation of scan rate and pH.

However, at pH= 14, peak to peak splitting and peak difference both are greater than 180mV with the scan rate. Thus, electrochemical reversibility is changing from reversible to irreversible with the reduction in pH. This reversibility mechanism is discussed in detail in the later section. As observed in Fig. 5.4(a), onsets of oxidation and reduction potentials are

observed to vary with pH. Thus, free energy of electrons varies from equilibrium position and this pH variation around oxygen ions alters the electronic energy of molecules. This leads to the alteration in HOMO and LUMO states.

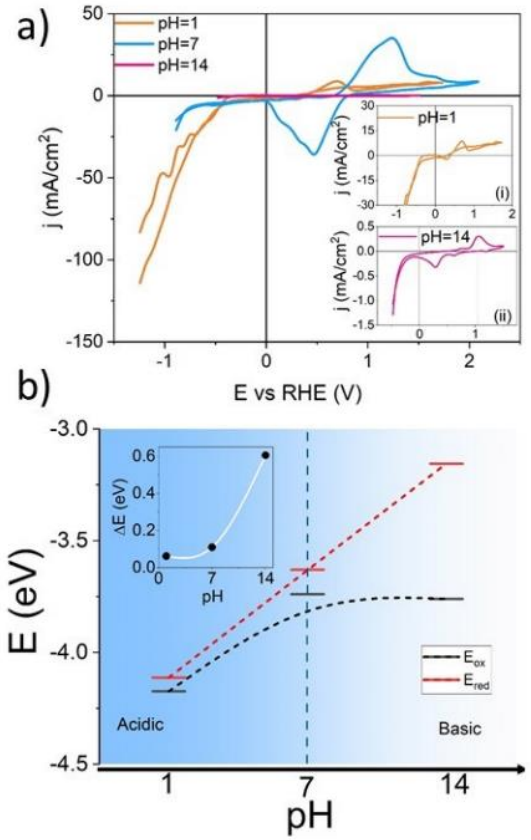

Figure 5.4 (a) Cyclic voltammograms with the variation of pH at 10 mV/sec scan rate, inset **(i)** Cyclic voltammogram at pH =1, inset **(ii)** Cyclic voltammogram at pH =14 **(b)** variation of HOMO and LUMO states with pH **(b)** inset variation of difference of HOMO and LUMO states ($\triangle \boldsymbol{E}$) with pH.

Fig. 5.4(b) shows the variation of HOMO and LUMO states [205] and inset shows the difference of HOMO and LUMO states, $(\triangle E)$, is steadily increasing with pH. It is observed that the onset of reduction potential is continuously increasing with the increase in pH whereas the onset of oxidation potential first increases up to pH=7 and thereafter, with the further

increase in pH, it becomes steady leading to the steady polarization. Now in the next sections, there is detail discussion about reversibility mechanism and alteration of potentials.

5.3.3 Electrochemical irreversibility

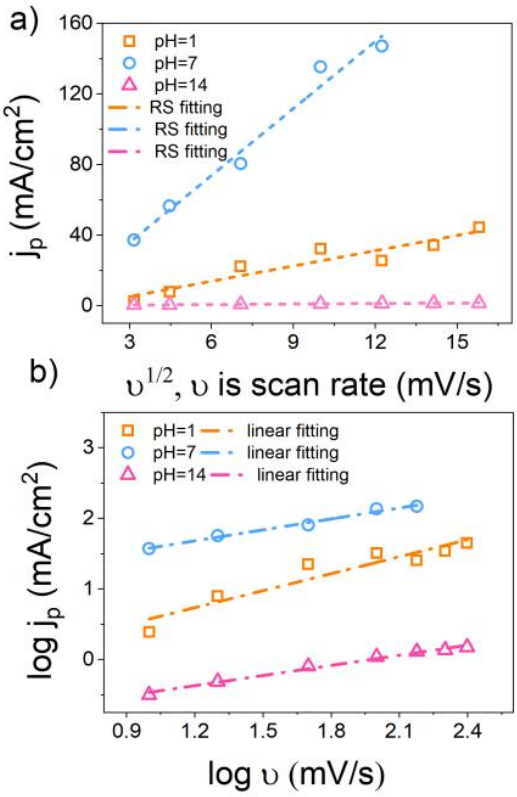

Figure 5.5 (a) R-S equation plot between the current density and υ with pH variation **(b)** log-log plot of current density and υ with pH variation.

The electrochemical reversibility is varied using the linear fitting of the peak current density, j_p versus $\upsilon^{1/2}$ via Randles Selvick (R-S) equation discussed in the previous section (equation 3.3)[163].

Fig. 5.5(a) shows the linear R-S plots suggest the faradaic currents flow via charge transfer. However, charge transfer occurs via diffusion and adsorption takes place via desorption. At pH=1, the slope of log-log plots of j_p versus υ, shown in Fig. 5.5(b) is 0.81 showing the failure of the adsorption equation and suggesting charge transfer via diffusion. With the increase in

pH, the slope, b value of log-log plots of j_p versus v reduces to 0.51 for pH = 7 and 0.47 for pH = 14, respectively suggesting the charge transfer via adsorption equation[158]-

$$j_p = i_p / a = \frac{n^2F^2}{4RT} v^b a\Gamma_o \tag{5.4}$$

where Γ_o is the surface covered under adsorbed surfaces and others have usual meanings discussed in previous chapters.

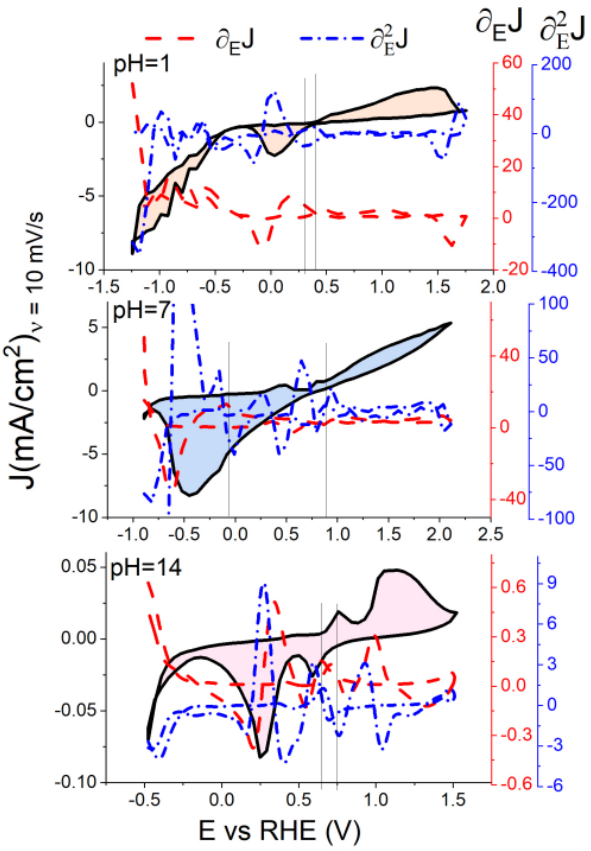

Figure 5.6 Current density, first- and second-order derivative CV curves at 10 mV/sec for the estimation of the parameters $\boldsymbol{E_{p/2}}$ and $\boldsymbol{E_i}$ with the variation of scan rate and pH.

In order to estimate the irreversibility or reversibility with pH variation, half-peak potential $E_{p/2}$ and inflection point potential E_i are estimated from the first- and second-order derivative of forward scans of CV curves (Fig. 5.6)[185]. It can be seen that forward and reverse scan

peaks are not exactly overlapped and are shifting towards lower potential suggesting the change in reversibility mechanism with pH variation [206][204].

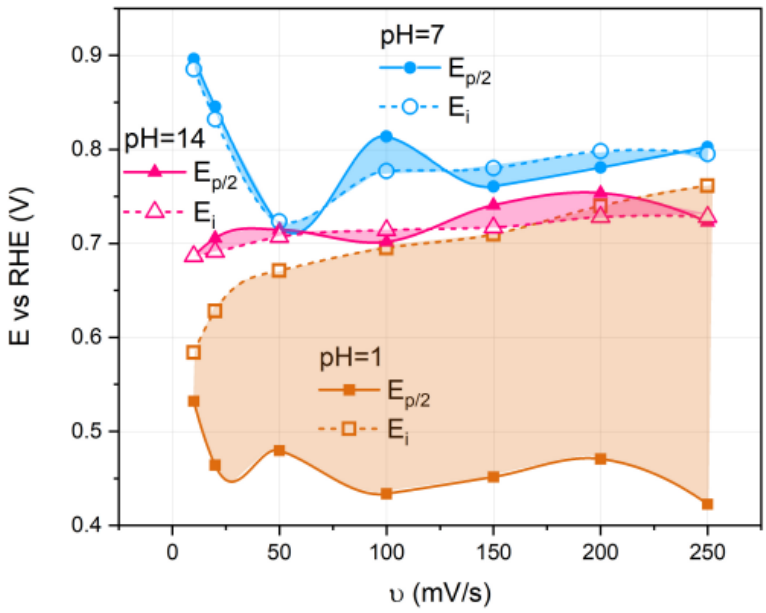

Figure 5.7 $E_{p/2}$ and E_i, estimated from the first- and second-order derivative of forward scans of CV curves (Fig 5.3) are with the scan rate for pH variation.

$E_{p/2}$ and E_i are plotted with the scan rate for pH variation (Fig. 5.7). It can be seen that at pH = 7 and 14, $E_{p/2}$ and E_i are nearly overlapping with each other while at pH=1, $E_{p/2}$ and E_i are not overlapping with each other. This suggests the conversion of reversibility to irreversibility with the decrease in pH variation.

5.3.4 Transient Response at interface

Figure 5.8 depicts transient current decay time estimated from the exponential decay fitting of chronoamperometric response with pH. It shows the time of 42.77 seconds in alkaline solvent, hereas, the time of 17.54 second is recorded in neutral medium.

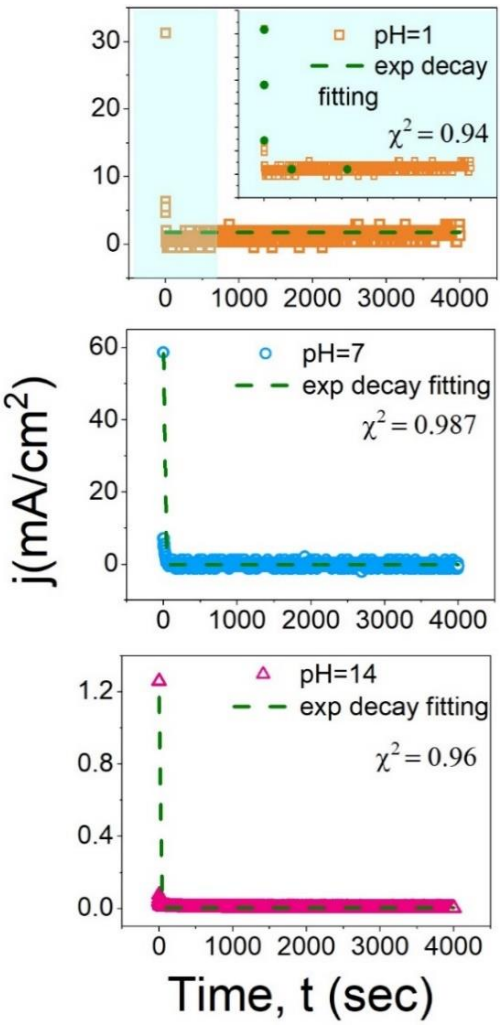

Figure 5.8 Chronoamperometric curve of current density and time with pH variation.

In order to estimate the transient current decay time, the current density is fitted with the exponential decay equation-

$$j = j_o + Aexp(-t/t_o) \tag{5.5}$$

where j_o and t_o are the characteristic current and time. A represents a constant which has the dimensions of current density. At pH=1, there is high transient time to achieve steady current at 4000 seconds but for a shorter duration of 1000 s, steady current is achieved in 0.61 seconds. This suggests the failure in achieving long term steady current at pH=1. Thus, neutral

(pH=7) and alkaline (pH=14) mediums are highly suitable for hole transport due to less transient response.

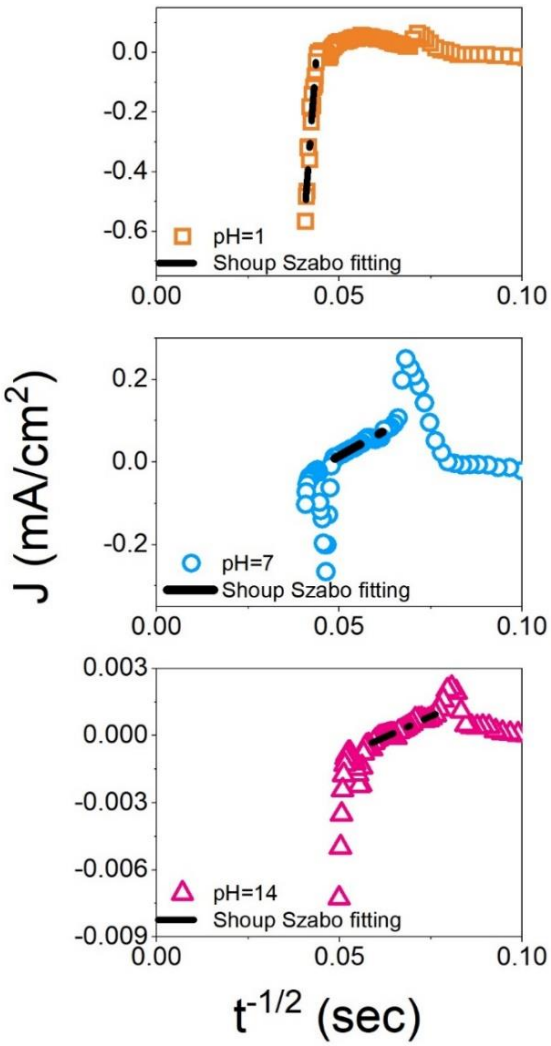

Figure 5.9 Shoup-Szabo fitting with pH variation.

Figure 5.9, j vs $t^{-1/2}$ is used to estimate the number of charge transfer and diffusion coefficient are estimated from from Shoup-Szabo relation discussed previously (equation 3.2)[163].

Table 5.1 Electrochemical parameters of samples at 300 K.

pH	D(m^2sec^{-1})	n	V_{FB} (V)	N_d
1	1.74×10^{-9}	6	0.81	2.24×10^{21}
7	7.40×10^{-12}	3	1.39	8.03×10^{18}
14	1.39×10^{-8}	6	1.37	2.65×10^{13}

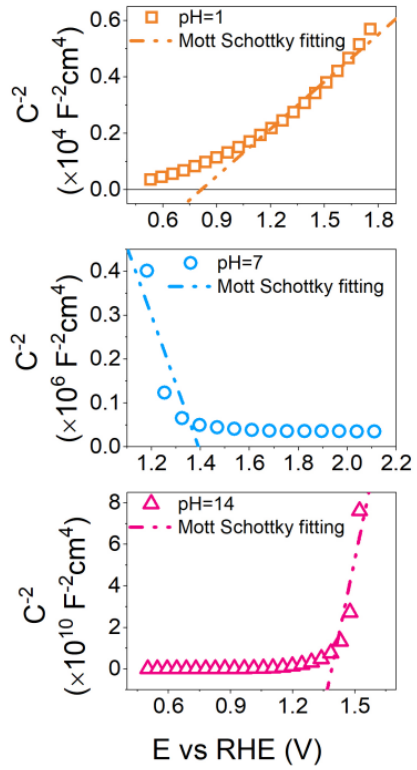

Figure 5.10 Mott Schottky fitting with pH variation suggesting n-type behavior in pH =1 and 14 while p-type behavior is observed in pH=7.

The estimated number of electron transfers is 6 for pH=1 and 14 while for pH=7, n =3. The diffusion coefficients estimated are shown in Table 5.1.

Figure 5.10 shows the Mott-Schottky plot [207] [201] and p-type nature is observed in pH=7 while a n-type nature is observed in both pH = 1 and 14. The charge concentration is highest in pH=1 and lowest in pH = 14. The flat band potential, V_{FB}, estimated from Mott- Schottky plots is mentioned in Table 5.1. The density of charge carriers is estimated using Mott-Schottky relation with permittivity, ε = 3.24.

5.3.5 Stability Test

In Fig. 5.11, the cycle stability is tested for 600 cycles in neutral medium (pH = 7). It is observed that the peak current in ORR and OER regimes have not varied till 600 cycles. However, 1st cycle, is activation cycle due to inertial potentials which is ideally not taken into consideration for any energy output. Constant current chronopotentiometry stability was observed in all media, material was not only unstable but also degrades within 1500 s in acidic and alkaline media.This is in accordance with the chronoamperometry measuremets where it was not feasible to achieve steady state current in 2000 s.

However, the system was quite stable in environment friendly neutral medium (Fig. 5.12). Fig. 5.12(a) shows stability for LSFT up to 1500 h in neutral media (pH =7) with a potential of 2V for current 150 mA/cm^2. Moreover, even for lower current density as low as 10 mA/cm^2 the cell potential deviation is only on the fourth decimal place shown in Fig. 5.12(b) [201][208].

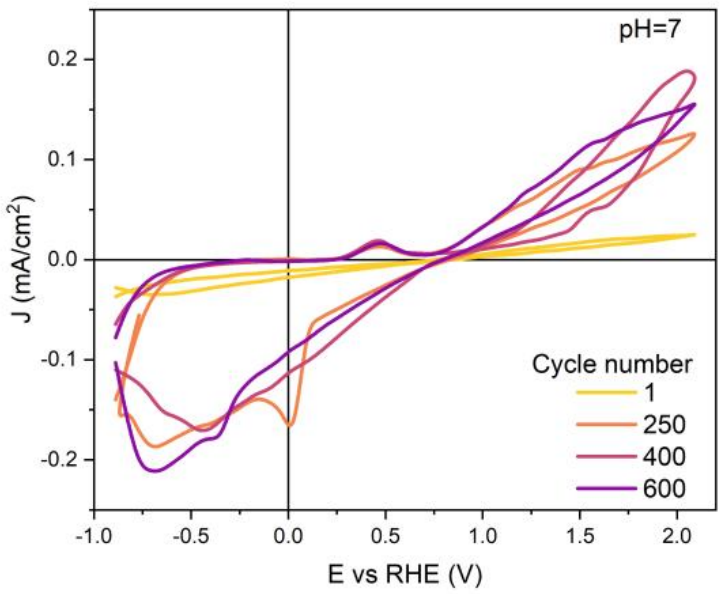

Figure 5.11 Cycle Stability of LSFT for 600 cycles in neutral media (pH =7).

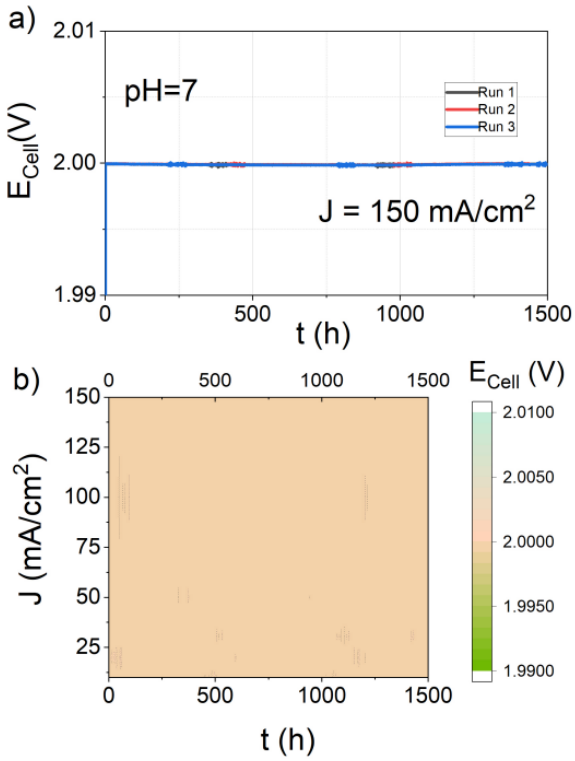

Figure 5.12 (a) Stability for LSFT up to 1500 h in neutral media (pH =7) with cell potential of 2V for current 150 mA/cm^2 **(b)** Current density and potential plot over a range of 1500 h.

However, the potentials are dependent on the nature of electrolyte, solvent, temperature, additives and processing conditions. In order to compare (refer to Fig 5.13), it has been prepared keeping the same processing conditions of perovskites i.e., solid state reaction route and from above findings it was concluded that LSFT is robust, efficient and biocompatible bifunctional catalyst due to high conductivity, catalytic current, and high chronopotentiometry stability.

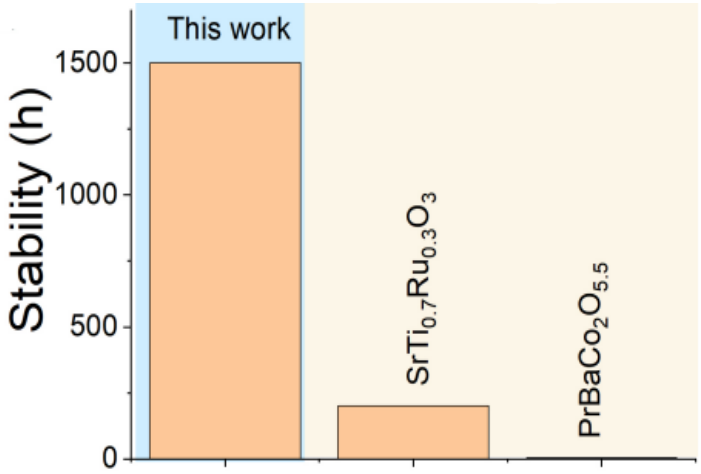

Figure 5.13 chronopotentiometric stability of 1500 h as compared to other neutral pH bifunctional catalysts.

5.4 Conclusion

The present study reports the first time synthesis $La_{0.5}Sr_{0.5}Fe_{0.5}Ti_{0.5}O_3$ (LSFT) is explored as a bifunctional catalyst for the simultaneous OER and ORR mechanism over a wide pH range. Higher current density in OER and ORR regimes with higher stability is observed in neutral medium. Also, this suggests its application as a robust and efficient neutral bifunctional environment-friendly catalyst due to high conductivity, catalytic current, and more than 1500 h chronopotentiometry stability with a potential of 2 V (vs Ag/AgCl) at a higher current of 150 mA/cm^2.